nanomaterials

MDPI

Article

Fabrication of Porous Lead Bromide Films by Introducing Indium Tribromide for Efficient Inorganic $CsPbBr_3$ Perovskite Solar Cells

Xianwei Meng [1], Kailin Chi [2,*], Qian Li [3], Bingtao Feng [1], Haodi Wang [4], Tianjiao Gao [4], Pengyu Zhou [2], Haibin Yang [1] and Wuyou Fu [1,*]

[1] State Key Laboratory of Superhard Materials, College of Physics, Jilin University, Changchun 130012, China; xwmeng17@mails.jlu.edu.cn (X.M.); fengbt20@mails.jlu.edu.cn (B.F.); yanghb@jlu.edu.cn (H.Y.)
[2] School of Science, Northeast Electric Power University, Jilin 132012, China; 20162715@neepu.edu.cn
[3] Beijing Key Lab of Cryo-Biomedical Engineering and Key Lab of Cryogenics, Technical Institute of Physics and Chemistry, Chinese Academy of Sciences, Beijing 100190, China; liqian@mail.ipc.ac.cn
[4] College of Physics, Jilin University, Changchun 130012, China; hdwang20@mails.jlu.edu.cn (H.W.); gaotj19@mails.jlu.edu.cn (T.G.)
* Correspondence: kailinchi@neepu.edu.cn (K.C.); fuwy@jlu.edu.cn (W.F.); Tel./Fax: +86-0432-64806674 (K.C.); +86-431-8516-8763-801 (W.F.)

Abstract: In the process of preparing $CsPbBr_3$ films by two-step or multi-step methods, due to the low solubility of CsBr in organic solvents, the prepared perovskite films often have a large number of holes, which is definitely not conducive to the performance of $CsPbBr_3$ perovskite solar cells (PSCs). In response to this problem, this article proposed a method of introducing $InBr_3$ into the $PbBr_2$ precursor to prepare a porous $PbBr_2$ film to increase the reaction efficiency between CsBr and $PbBr_2$ and achieve the purpose of In (III) incorporation, which not only optimized the morphology of the produced $CsPbBr_3$ film but also enhanced the charge extraction and transport capabilities, which was ascribed to the reduction of the trap state density and impurity phases in the perovskite films, improving the performance of $CsPbBr_3$ PSCs. At the optimal $InBr_3$ concentration of 0.21 M, the $InBr_3$:$CsPbBr_3$ perovskite solar cell exhibited a power conversion efficiency of 6.48%, which was significantly higher than that of the pristine device.

Keywords: $CsPbBr_3$; perovskite solar cells; $InBr_3$; $PbBr_2$; incorporation

Citation: Meng, X.; Chi, K.; Li, Q.; Feng, B.; Wang, H.; Gao, T.; Zhou, P.; Yang, H.; Fu, W. Fabrication of Porous Lead Bromide Films by Introducing Indium Tribromide for Efficient Inorganic $CsPbBr_3$ Perovskite Solar Cells. *Nanomaterials* **2021**, *11*, 1253. https://doi.org/10.3390/nano11051253

Academic Editor: Seok-In Na

Received: 21 April 2021
Accepted: 8 May 2021
Published: 11 May 2021

1. Introduction

After more than ten years of rapid development, lead halide-based perovskite solar cells have made remarkable achievements, but they seem to be in a vicious circle where high efficiency and high stability are contradictory to each other. Although the power conversion efficiency (PCE) of organic-inorganic hybrid perovskite solar cells (PSCs) has increased from the initial 3.8% to more than 25% at present [1–5], yet due to the strong volatility of common A-site organic cations, such as organic methylammonium (MA^+) and formamidinium (FA^+), the organic components disappear under thermal stress [6,7]. In terms of thermal stability, the all-inorganic cesium-lead halide perovskite $CsPbX_3$ (X: iodine or bromine), which is formed by using more stable inorganic cesium ions (Cs^+) to completely replace organic cations, usually performs better stability [8–11] and is not prone to degradation at temperatures above 400 °C [8,12]. This provides the necessary conditions for the long-term stable use of $CsPbX_3$ PSCs [13–16]. The key factor, which influences the stability of $CsPbX_3$, is the moisture in the air. The presence of humidity changes the phase of the perovskite and reduces the stability of the photovoltaic device, but this does not directly cause the decomposition of $CsPbX_3$ (mainly I-rich $CsPbX_3$) and the lack of components [8,17,18]. Of course, this phase change is reversible when heated [19].

Compared with other Cs-based inorganic perovskites, the most prominent advantage of $CsPbBr_3$ is that it has a highly stable crystal structure. Whether it is the orthorhombic γ-phase at room temperature or tetragonal β-phase and cubic α-phase when heated, the geometric structures of $CsPbBr_3$ have not changed much, so the electronic structures of different phases are also relatively similar [20]. For this reason, $CsPbBr_3$ is also regarded as a perovskite material that presents better stability to humidity, heat, and light at ambient temperature [2,8,21,22]. Since Kulbak et al. first prepared the $CsPbBr_3$ PSCs by a two-step solution-processing method in 2015 [22], in less than ten years, the PCE of the $CsPbBr_3$ based PSCs have reached more than 10% with an ultrahigh open-circuit voltage (V_{OC}) of 1.62 V [23], but it still has a large distance compared with $CsPbBr_3$ PSCs theoretical limit PCE of 16.4% [24] and the maximized PCE of 19.0% for inorganic $CsPbI_3$ PSCs [10].

In the process of preparing $CsPbBr_3$ PSCs by the solution-processing method, the solubility of CsBr in commonly used polar solvents is poor, and the concentration differences between CsBr and $PbBr_2$ solutions are large, which leads to the derivative phases $PbBr_2$-rich $CsPb_2Br_5$ and CsBr-rich Cs_4PbBr_6 in the process of the generation of $CsPbBr_3$ [25]. At the same time, the thickness of the non-optimized prepared perovskite film is low, and the ability to absorb light is inadequate; numerous pinholes appear in the film [26]. Consequently, a decrease appears in the PCE of $CsPbBr_3$ PSCs. Regardless of whether it is a two-step sequential deposition or a multi-step method to prepare $CsPbBr_3$, it is necessary to deposit $PbBr_2$ first and then use CsBr to convert $PbBr_2$ to $CsPbBr_3$. Improving the $PbBr_2$ film preparation process and adjusting the $PbBr_2$ preparation method can achieve the goals of enhancing the reaction efficiency of the precursor, accurately controlling the subsequent growth of $CsPbBr_3$ crystals, and reducing the generation of by-products, and finally obtain perovskite film with a high purity phase, large grain size, and high coverage [23,27]. By precisely regulating the film-forming temperature and pore diameter of the $PbBr_2$ precursor film, Zhao et al. [23] minimized the compressive stress of the perovskite film and prepared $CsPbBr_3$ grains with a size of up to 1.62 μm, which not only made the PCE of the all-inorganic $CsPbBr_3$ perovskite solar cell reach 10.7%, the open-circuit voltage (V_{OC}) as high as 1.6 V, and it also kept the device extremely stable in a high-humidity air environment. Lee et al. [28] introduced CZISSE QDs quantum dots into the $PbBr_2$ film. CZISSE QDs acted as seeds to promote the crystallization of $CsPbBr_3$ and, at the same time, penetrated into the m-TiO_2 and $CsPbBr_3$ perovskite films to increase the electron extraction and transportability of TiO_2, thereby improving the conversion efficiency of the device by 20.6%.

In this work, $InBr_3$ was introduced into the $PbBr_2$ precursor solution, so that the multiple ordered crystal orientations of lead bromide grew, and the original rough and extremely uneven grain distribution of the $PbBr_2$ film evolved into a large uniform-porous film with pores. This morphological change ensured the full diffusion and uniform reaction of CsBr in the $PbBr_2$ film during the synthesis of $CsPbBr_3$ and was conducive to the formation of polycrystalline surface growth, high purity phase, and uniform morphology $InBr_3$: $CsPbBr_3$ film. The PCE of the small area (0.09 cm^2) $InBr_3$:$CsPbBr_3$ PSC obtained after conditions optimization was 6.48%, in particular, the V_{OC} was significantly improved.

2. Experiment Section

2.1. Materials

$PbBr_2$ (99.99%) and CsBr (99.9%) were purchased from Xi'an Polymer Light Technology Corp. (Xi'an, China) and were not purified. $InBr_3$ (99.9%) was purchased from Shanghai Macklin Biochemical Co., Ltd. (Shanghai, China). Titanium diisopropoxide bis (acetylacetonate; 75 wt% in 2-propanol) was purchased from Sigma-Aldrich (Louis, MO, USA). Titanium dioxide (TiO_2) paste (18 NR-T) was purchased from Greatcell Solar Limited (Queanbeyan, Australia). N,N-Dimethylformamide (DMF, chromatographic grade, ≥99.9%), methanol (chromatographic grade, ≥99.9%), ethanol (chromatographic grade, ≥99.8%), and isopropanol (≥99.5%) were purchased from Aladdin (Shanghai, China). The fluorine-doped tin oxide coated glass (FTO, 6 Ω/□) and carbon paste were purchased from

Opvtech New Energy Co., Ltd. (Yingkou, China) and Shanghai MaterWin New Materials Co., Ltd. (Shanghai, China), respectively.

2.2. Device Fabrication

All the following processes were carried out in a fume hood environment, without artificial control of the temperature, humidity, and airflow rate of the surrounding environment. The fluorine-doped tin-oxide-coated glasses were patterned by laser etching and cleaned by ultrasonic with acetone, isopropanol, ethanol, and deionized water. After being dried by high purity nitrogen, the FTO were further cleaned by an ultrasound treatment for 15 min and washed with ethanol. Afterward, the pre-conditioned FTO were spin-coated with 0.15 M titanium diisopropoxide bis(acetylacetonate) in 1-butanol at 5000 rpm for 20 s and were heated at 125 °C for 5 min. After these substrates returned to room temperature, the above procedure was repeated twice with 0.3 M titanium diisopropoxide bis(acetylacetonate) in 1-butanol and compact TiO_2 (c-TiO_2) was obtained. After that, the mesoporous TiO_2 (m-TiO_2) films were deposited on the above cooling c-TiO_2 by spin-coating at 5000 rpm for 30 s by means of TiO_2 paste diluted with ethanol. Further, the obtained layers were dried at 125 °C for 5 min followed by the muffle furnace at 500 °C for 30 min. After the muffle furnace was lowered to room temperature, pre-coated substrates were acquired.

Perovskite films were synthesized by a multistep solution-processing method. 0.03, 0.09, 0.15, 0.21, and 0.27 mmol $InBr_3$ were added into 1 mL DMF of $PbBr_2$ (1 M) and stirred. After the $InBr_3$ was completely dissolved, the DMF mixed solution was spin-coated on pre-coated substrates at 2000 rpm for 30 s and then heated to 90 °C for 30 min. Afterward, the methanol solution of CsBr (0.07 M) was spin-coated on the $InBr_3$:$PbBr_2$ film at 5000 rpm for 30 s and heated to 250 °C for 5 min, and this step was repeated five times. Next, the prepared sample was placed in isopropanol and soaked for 30 min and annealed at 250 °C for 15 min to remove excess CsBr. Finally, the carbon paste was deposited coated on the perovskite films by using the doctor blade coating method and dried at 100 °C for 10 min. The effective area of the back electrode was 3 mm × 3 mm, which defined the active area of each device.

2.3. Characterization

The morphologies of the synthesized films and energy-dispersive X-ray spectroscopy (EDS) mapping images were observed by a scanning electron microscope (SEM, FEI MAGELLAN 400, FEI, Hillsboro, OR, USA). The crystal structure of the synthesized sample was determined by means of X-ray diffraction (XRD, Cu Kα radiation, λ = 1.5418 Å, Rigaku D/max2500, Tokyo, Japan). The steady-state photoluminescence (PL) spectra of perovskite films were performed using a Renishaw InVia micro-Raman spectroscopy system (Renishaw, Wotton-under-Edge, UK) with a 473 nm excitation source. Ultraviolet photoelectron (UPS) and X-ray photoelectron spectroscopy (XPS) were carried out by an X-ray photoelectron spectrometer (EscaLab Xi+, Thermofisher, Waltham, MA, USA). UV-Vis spectrometer (UV-3600, Shimadzu, Kyoto, Japan) was employed to measure the absorption spectrum in the range of 200 nm to 800 nm. The current-voltage (*J*–*V*) characteristics and the external quantum efficiency (EQE) of the fabricated solar devices were measured by a solar cells test system (XP3000, Sanyou, Beijing, China) and an EQE measured system (QTest Station 1000A, CROWNTECH, Inc., Macungie, PA, USA), respectively. The impedance was executed at 10^{-1}~10^{7} Hz by using an impedance analyzer in a dark environment (Solartron 1260 coupled to the dielectric interface 1296, Farnborough, UK).

3. Results and Discussion

In the two-step or multi-step method of preparation of perovskite, the quality of the $PbBr_2$ film determined the morphology of the following perovskite film. Figure 1 shows the top-view SEM images of $PbBr_2$ films by introducing different concentrations of $InBr_3$. When there was no $InBr_3$ in the $PbBr_2$ precursor solution, as shown in Figure 1a, the

surface of the obtained sample was rough, and the $PbBr_2$ grain distribution was extremely uneven, and a large area of exposed m-TiO_2 could be directly observed. When the $PbBr_2$ precursor solution was introduced into 0.03 M $InBr_3$, as shown in Figure 1b, the surface of the $PbBr_2$ film was flat, and the coverage of the m-TiO_2 film was increased, and the observable exposed m-TiO_2 area was significantly reduced. With the gradual increase in the concentration of introduced $InBr_3$ (Figure 1c–f), the $PbBr_2$ film appeared porous, but the number of pores decreased as the concentration of $InBr_3$ increased. Meanwhile, the porosity volume increased as the concentration of $InBr_3$ increased. From the cross-sectional view of $PbBr_2$ shown in Figure S1 (Supplementary Materials), we could clearly see that the pure $PbBr_2$ film has a flat surface and a uniform thickness of about 50~60 nm, and the m-TiO_2 was filled with $PbBr_2$. As the concentration of $InBr_3$ introduced gradually increased, the thickness of the $PbBr_2$ film also gradually increased (about 70 nm, 90 nm, 100 nm, 120 nm, 160 nm), and the film roughness increased. The above data could clearly demonstrate that the introduction of $InBr_3$ could effectively affect the morphology of the $PbBr_2$ film. The increase in the porosity volume, roughness, and thickness of the $PbBr_2$ film facilitated the diffusion of the subsequent CsBr solution, increased the reaction efficiency with CsBr, and then achieved the full growth of $CsPbBr_3$ grains [29,30].

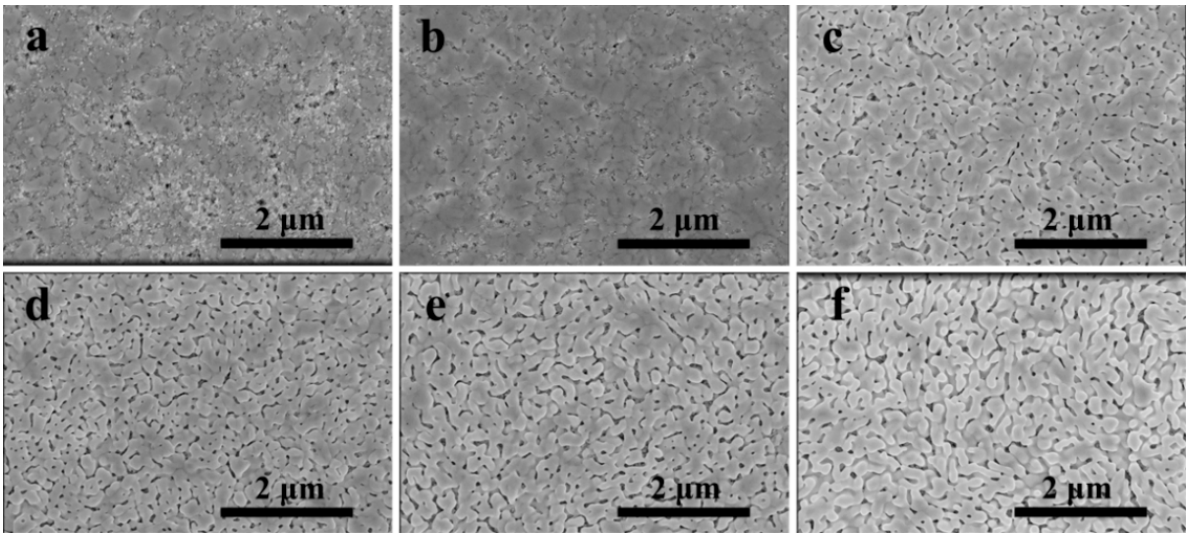

Figure 1. Top-view scanning electron microscope (SEM) images of $PbBr_2$ films by introducing different concentrations of $InBr_3$: (**a**) 0.00 M; (**b**) 0.03 M; (**c**) 0.09 M; (**d**) 0.15 M; (**e**) 0.21 M; (**f**) 0.27 M.

To investigate the influence of $InBr_3$ on the structure of $PbBr_2$, XRD patterns of $InBr_3$:$PbBr_2$ films are shown in Figure 2a. It could be seen that Pure $PbBr_2$ was in the orthorhombic phase crystal structure (PDF#84-1181) [23]. When $InBr_3$ was introduced, for all concentrations of $InBr_3$ used, two new diffraction peaks of (011) and (200) crystallographic planes of $PbBr_2$ could be found at 2θ of 20.94° and 22.05°, but no diffraction peak belonging to $InBr_3$ or other protobromides were found. Since $InBr_3$ did not exist in the form of simple In^{3+} and Br^- in the DMF solution, it was self-ionized and formed various complexes [31–33]. Therefore, we speculated that in the process of $PbBr_2$ crystal growth, In (III) could be in the form of free In^{3+} to replace a part of the Pb vacancy or exchange it with Pb, or the In cluster was directly bound to host lattice constituents [33–35]. Meanwhile, the $PbBr_2$ crystal was made to grow along multiple ordered crystal orientations. When using the XPS technique to prove the presence of In in $PbBr_2$ films, not surprisingly, characteristic peaks belonging to Br 3d, Pb 4f, and In 3d were found in the XPS spectra for the pure $PbBr_2$ and $InBr_3$:$PbBr_2$ films, as shown in Figure 2b. According to Figure 2c–e, the core level $In3d_{5/2}$ and $3d_{3/2}$ were located at 445.4 eV and 452.9 eV, respectively, and the Pb $4f_{5/2}$ and $4f_{7/2}$ peaks in Pb 4f spectrum and Br $3d_{3/2}$ and $3d_{5/2}$ peaks in Br 3d spectrum all moved towards higher binding energies, which showed that Pb-Br interactions were enhanced after In^{3+} or In

cluster incorporation [36]. Additionally, the EDS mapping was also utilized to confirm the presence of In in the $InBr_3$:$PbBr_2$ films. Figure S2 (Supplementary Materials) demonstrated that all elements were uniformly distributed in the corresponding film, especially, there was no aggregation of In elements.

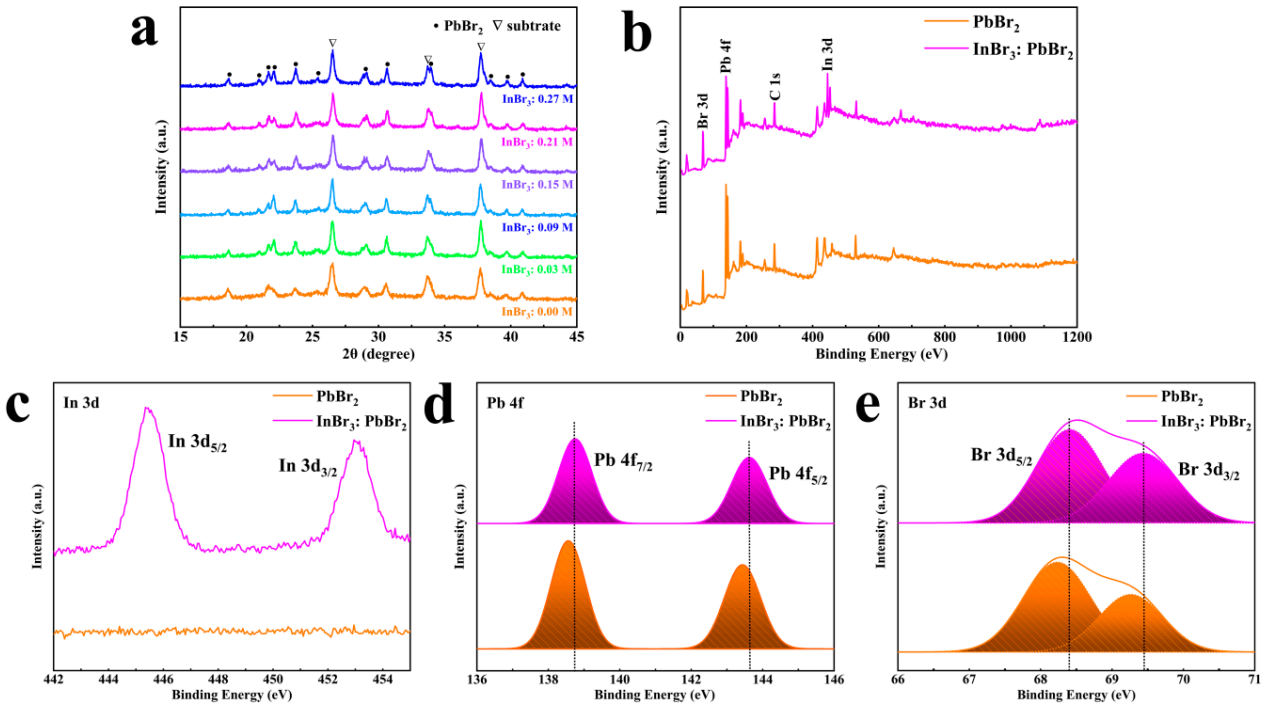

Figure 2. (**a**) X-ray diffraction (XRD) patterns of $PbBr_2$ films by introducing different concentrations of $InBr_3$. (**b**) X-ray photoelectron spectroscopy (XPS) spectra, and (**c**) In 3d, (**d**) Pb 4f, (**e**) Br 3d XPS core spectra of $InBr_3$:$PbBr_2$ film.

Figure 3 depicts the top-view SEM images of perovskite films without and with $InBr_3$ with the corresponding cross-section SEM images inserted in the inset. The size of the crystal grain of the pure $CsPbBr_3$ was quite different, the film uniformity and coverage were also bad, and the bare m-TiO_2 could be clearly seen. As the concentration of introduced $InBr_3$ gradually increased (0.03~0.21 M), the coverage of m-TiO_2 by $CsPbBr_3$ films also gradually increased, and the size and number of pores in each film showed a downward trend. This morphological change was conducive to the performance of the perovskite cells. However, when the concentration of $InBr_3$ was further increased by 0.27 M, there were again obvious holes in the $CsPbBr_3$ film. This result indicated that the quality and surface $CsPbBr_3$ film depended on the morphology of the corresponding porous $InBr_3$:$PbBr_2$ film greatly that was, the morphology of $CsPbBr_3$ film could be modified by changing $InBr_3$ concentration.

The XRD patterns shown in Figure 4a revealed that all $CsPbBr_3$ films had a cubic structure (PDF#54-0752) [23], and the positions of the diffraction peaks were not significantly shifted to high or low angles, which demonstrated that, although In cluster could promote growth along multiple ordered crystal orientations, it could not change the phase of $CsPbBr_3$. When the concentration of the introduced $InBr_3$ was 0.00 M and 0.03 M, there existed two peaks located at 11.7° and 29.4°, respectively, which belonged to (002) and (213) lattice planes of the $CsPb_2Br_5$ phase [37]. As the concentration of $InBr_3$ was further increased (0.09~0.27 M), no obvious impurity peak belonging to $CsPb_2Br_5$ or Cs_4PbBr_6 phase could be observed. In fact, the control of the reaction rate between CsBr and $PbBr_2$ was a necessary condition for preparing $CsPbBr_3$ films with a high purity phase and high coverage. Based on Figure 1, the appropriate concentration of $InBr_3$ could make the $PbBr_2$ film have higher porosity, which provided more effective diffusion paths for the diffusion of CsBr methanol solution in the $PbBr_2$ film, and appropriately increased the contact area

between CsBr and $PbBr_2$. That could also ensure the full growth of $CsPbBr_3$ crystal grains and, at the same time, could prevent the formation of the impurity phase due to excessive $PbBr_2$ or CsBr. However, if the concentration of the $InBr_3$ introduced into $PbBr_2$ was too low or too high, it was not conducive to controlling the reaction rate of CsBr and $PbBr_2$. In the process of the reaction, due to the incomplete reaction of the precursors or the excessive growth of crystal grains, the morphology of the $CsPbBr_3$ film was easily deteriorated, accompanied by the formation of byproducts. Further XPS was employed to certify the presence of the incorporated In^{3+} in the $InBr_3$:$CsPbBr_3$ film. Figure S3 (Supplementary Materials) exhibited the XPS of Cs 3d, Pb 4f, Br 3d, and In (III) 3d for the $CsPbBr_3$ and the $InBr_3$:$CsPbBr_3$ films, respectively. As seen in Figure 4b, compared with $CsPbBr_3$ film, two In signals corresponding to In $3d_{5/2}$ and $3d_{3/2}$ core levels were detected in $InBr_3$:$CsPbBr_3$ film, and Cs 3d, Pb 4f, and Br 3d all moved towards higher values, which means that the chemical state of the $[PbBr_6]^{4-}$ octahedral was altered and Pb-Br and Cs-Br interactions were enhanced after replacing Pb^{2+} (1.7497 Å) with In^{3+} (1.6590 Å) with a smaller ion radius accompanied by the size of the $[PbBr_6]^{4-}$ octahedral and the voids decreased [35]. The contraction of lattice and the enhancement of the spatial symmetry of the crystal structure caused by the incorporation of In^{3+} or In cluster could result in an efficient charge transport along with multiple directions, which perhaps was one of the important factors to improve the performance of $CsPbBr_3$ cells [35,38]. The EDS mapping was used to characterize the cross-sectional of $InBr_3$:$CsPbBr_3$, and it was confirmed that In was evenly distributed inside the perovskite, which indicated the successful incorporation of $CsPbBr_3$ by In (Figure S4, Supplementary Materials).

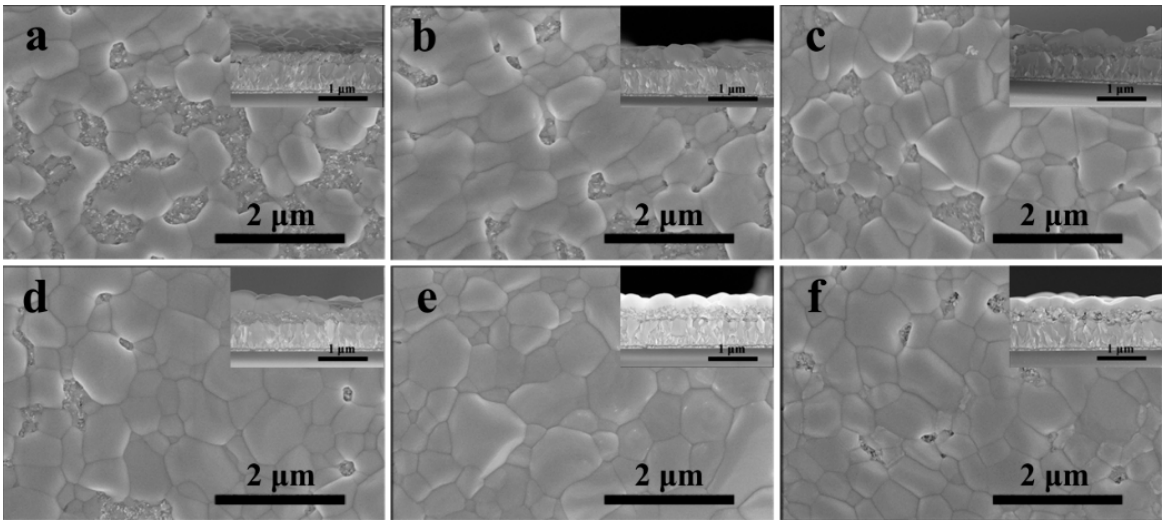

Figure 3. Top-view and cross-sectional (insets) SEM images of $CsPbBr_3$ films by introducing different concentrations of $InBr_3$: (**a**) 0.00 M; (**b**) 0.03 M; (**c**) 0.09 M; (**d**) 0.15 M; (**e**) 0.21 M; (**f**) 0.27 M.

Subsequently, UV-vis Spectrometer, UPS, PL were used to characterize the cells with the FTO/c-TiO_2/m-TiO_2/$CsPbBr_3$ structure. Figure S5a (Supplementary Materials) shows the absorption spectra of the $CsPbBr_3$ with different concentrations of $InBr_3$. The absorption edge of each perovskite film was at approximately 530 nm within the visible region, which revealed that the concentration change of the introduced $InBr_3$ did not significantly affect the light absorption range of $CsPbBr_3$. Correspondingly, the calculated bandgaps (2.34 eV) did not reveal obvious and meaningful changes (Figure S5b, Supplementary Materials). As the concentration of $InBr_3$ increased, so did the film's capacity to absorb visible light. This was mainly attributed to the phase-purity of the perovskite film and the full growth of crystal grains, which was beneficial to improve the short current density (J_{SC}) of the cells. The mechanism of this phenomenon was mainly attributed to the partial substitution of Pb^{2+} by In^{3+} or In cluster [34,35]. Figure 5a,b present the UPS spectra

of the pristine and $InBr_3$ (0.21M):$CsPbBr_3$ films. By formula valence band maximum $E_{VBM} = 21.22\ eV - (E_{cutoff} - E_{onset})$ [39,40], it could be calculated that the valence band (E_V) of $CsPbBr_3$ and $InBr_3$:$CsPbBr_3$ were −5.60 and −5.28 eV, respectively, which was ascribed to the rearrangement of electrons outside the Cs, Pb, and Br atoms after the incorporation of In^{3+} or In cluster [34,35]. Combined with Figure S5b, the corresponding calculated conduction band (E_C) was −3.26 and −2.94 eV, and the energy band diagram of isolated semiconductors of the PSCs using carbon electrodes is plotted in Figure 5c [39,41]. For HTL-free PSCs, Ev of the perovskite should be deeper than the work function (W_F) of the carbon electrode [39] so as to facilitate the extraction of photogenerated holes and reduce the energy loss of the holes during the transmission process [39]. Obviously, the incorporation of In^{3+} or In cluster effectively reduced the difference in interface energy levels, thereby facilitating the charge extraction and transfer and enhancing the photovoltaic performance of PSCs. In addition, the PL was conducted to analyze the carrier transfer behavior of $CsPbBr_3$ and $InBr_3$:$CsPbBr_3$ films. As shown in Figure 5d, all perovskite films showed the typical emission band around 523 nm. $InBr_3$ (0.21 M):$CsPbBr_3$ film showed a strong quenching in contrast with the pristine and other $CsPbBr_3$ films introduced with $InBr_3$, which indicated that $InBr_3$ could effectively inhibit the carrier recombination and enhance the charge extraction ability. The main reason behind this was that the defect density caused by the pinholes of $CsPbBr_3$ films surface, and the impurity phase of $CsPbBr_3$ films are obviously improved by adding $InBr_3$, and the enhancement of the spatial symmetry of the crystal structure caused by partial substitution of Pb^{2+} by In^{3+} or In cluster [34,35,39,42].

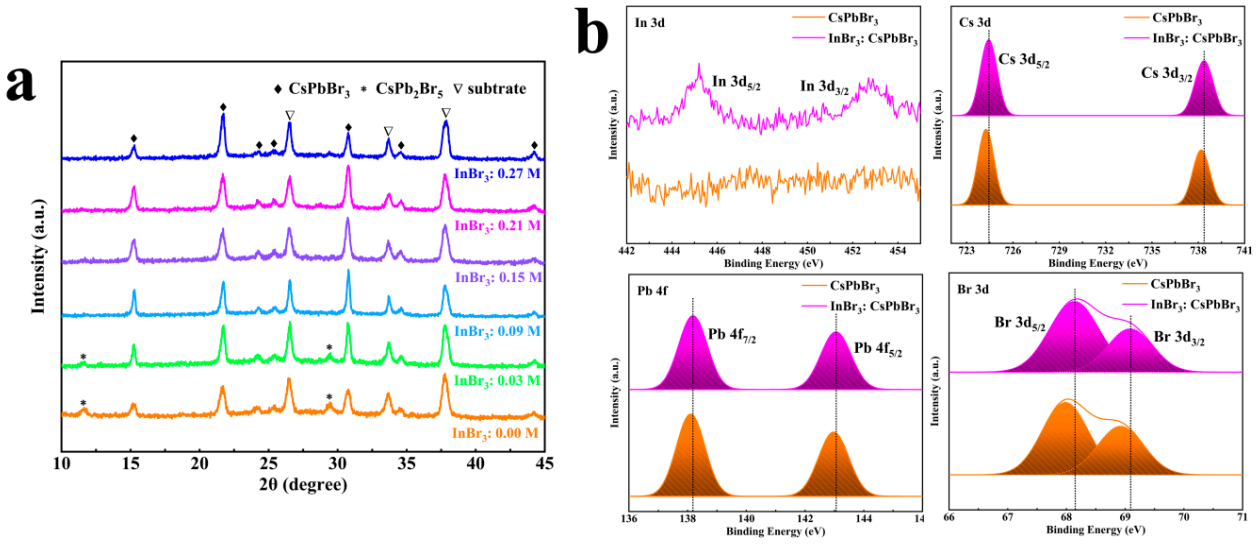

Figure 4. (**a**) XRD patterns of $CsPbBr_3$ films by introducing different concentrations of $InBr_3$. (**b**) In 3d, Cs 3d, Pb 4f, Br 3d XPS core spectra of $InBr_3$:$CsPbBr_3$ film.

The HTL-free PSCs were synthesized based on the standard mesoscopic architecture of c-TiO_2/m-TiO_2/$InBr_3$:$CsPbBr_3$/carbon, and the cross-section of the complete device is given in Figure 6a. The current *J*–*V* characteristics of relevant devices under reverse scanning are presented in Figure 6b, the corresponding forward scanning curve is shown in Figure S6 (Supplementary Materials), and the key parameters including Jsc, Voc, FF, PCE, and hysteresis index (HI) are summarized in Table 1. The PCE of all devices with $InBr_3$ introduced were better than that of the pristine ones, and all parameters showed a regular trend of first increasing and then decreasing with an increase of the concentration of $InBr_3$ introduced. When the concentration of $InBr_3$ was 0.21 M, the corresponding device exhibited the best performance. Compared with the pristine device, the PCE of $InBr_3$ (0.21 M):$CsPbBr_3$ device was significantly improved from 3.29% to 6.48% with the continuously increased J_{SC} of 4.21 and 6.52 mA/cm^2, Voc of 1.28 and 1.38 V, FF of 0.61 and 0.72, and HI of 0.25 and 0.03. When the $InBr_3$ concentration was further increased

to 0.27 M, the J_{SC} of the device dropped by about 0.5 mA/cm^2, while the Voc and FF did not change significantly, which was due to the deterioration of the $InBr_3$:$CsPbBr_3$ film morphology. The PEC of PSCs was determined by a variety of complex factors. According to the experimental results of SEM, UV-vis, UPS, and PL, the improvements of Voc and FF were due to the rise in the energy difference between the perovskite conduction band and electron transport layer, thereby reducing the energy loss of the holes in the transmission process. The improved Jsc was not only ascribed to the quality of the $InBr_3$:$CsPbBr_3$ film morphology or the increase in film coverage to absorb more photons to generate more electrons but also reduced vacancy defects in the optimized $CsPbBr_3$ films to improve the charge extraction and transfer process after the incorporation of In^{3+} or In cluster. In addition, the smaller hysteresis of the $InBr_3$:$CsPbBr_3$ cells performed than that of the pristine device might be enabled by the passivation function of $InBr_3$ to diminish the defects of Pb^{2+} and Br^- [34,35]. Figure 6c shows the external quantum efficiency (EQE) spectrum. The highest EQE value of 84% was achieved at the $InBr_3$ concentration of 0.21 M, whereas the reference devices with less or excessive $InBr_3$ concentration displayed lower EQE responses. This regular change was consistent with the results of *J*–*V* characteristics. Additionally, the integrated current density calculated by the EQE curve of each device was very close to the J_{SC}, and the mismatch was less than 5%. Figure 6d demonstrates the Nyquist plots of pristine $CsPbBr_3$ and $InBr_3$ (0.21 M):$CsPbBr_3$ devices measured at a reverse potential of 1.0 V and the corresponding equivalent circuit model. Table S1 (Supplementary Materials) also provides a list of the fitting values of the series resistance (R_s) and the charge recombination resistance (R_{rec}). After the introduction of $InBr_3$, R_{rec} increased from 765 to 1152 Ω, which showed that the incorporation of In had efficient repression of carrier recombination due to the significantly improved film formation quality of perovskites, thus reducing the trap state density and improving carriers mobility [39].

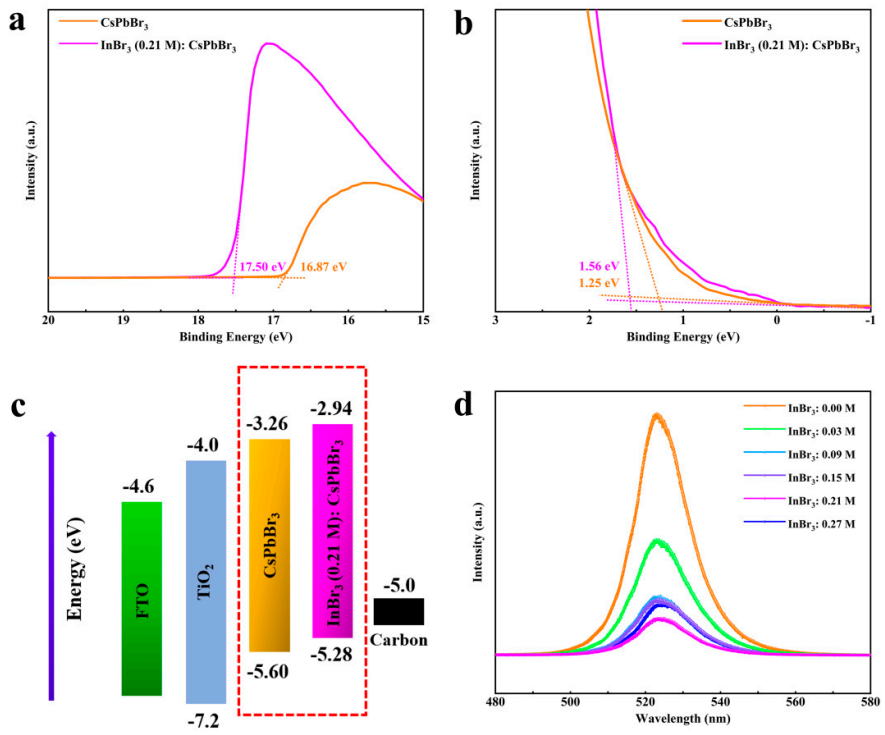

Figure 5. (**a**,**b**) UPS spectra of the pristine and $InBr_3$ (0.21 M):$CsPbBr_3$ films. The linear fittings indicate the photoemission cutoff energy boundary (E_{cutoff}) and onset (E_{onset}) values. (**c**) Energy level diagram for the carbon-based pristine and $InBr_3$ (0.21 M):$CsPbBr_3$ PSCs. (**d**) PL spectra of the cells by introducing different concentrations of $InBr_3$.

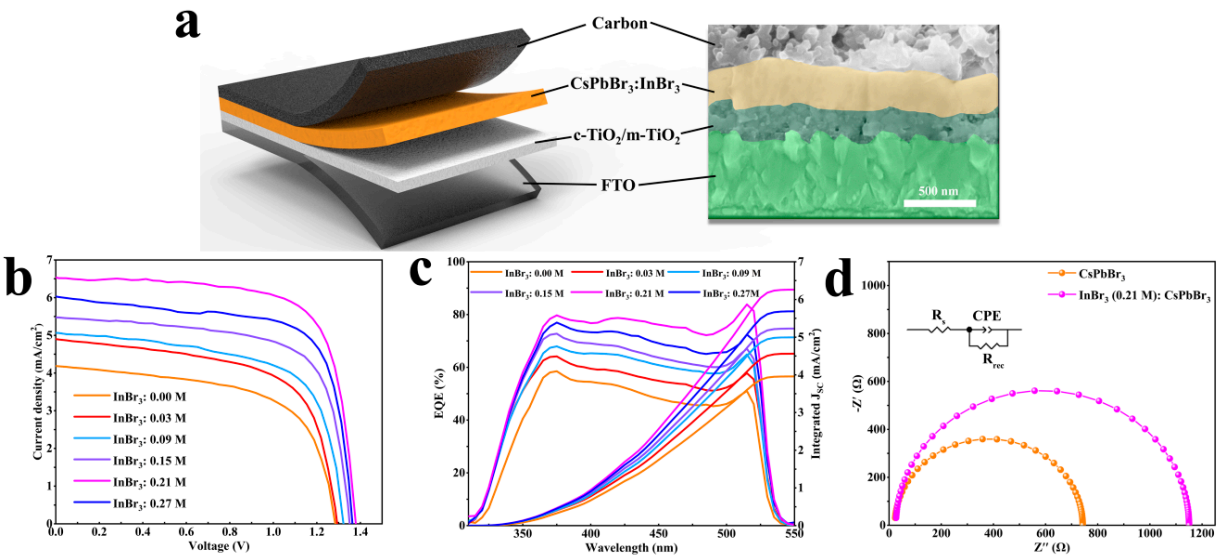

Figure 6. (**a**) Cross-sectional SEM image of the $InBr_3$:$CsPbBr_3$ device, (**b**) *J*–*V* characteristics, and (**c**) EQE spectra and integrated photocurrent densities for the $InBr_3$:$CsPbBr_3$ devices. (**d**) Nyquist plots of the pristine $CsPbBr_3$ and $InBr_3$ (0.21 M):$CsPbBr_3$ devices with the equivalent circuit depicted in the inset.

Table 1. Key *J*–*V* parameters of the $InBr_3$:$CsPbBr_3$.

Samples	Scan	J_{SC} (mA/cm^2)	V_{OC} (V)	FF	PCE (%)	HI
$InBr_3$: 0.00 M	Forward	4.05	1.27	0.48	2.46	0.25
	Reverse	4.21	1.28	0.61	3.29	
$InBr_3$: 0.03 M	Forward	4.82	1.27	0.53	3.24	0.17
	Reverse	4.87	1.29	0.62	3.90	
$InBr_3$: 0.09 M	Forward	5.14	1.31	0.59	3.97	0.09
	Reverse	5.08	1.32	0.65	4.36	
$InBr_3$: 0.15 M	Forward	5.45	1.33	0.64	4.63	0.08
	Reverse	5.49	1.35	0.68	5.04	
$InBr_3$: 0.21 M	Forward	6.49	1.37	0.71	6.31	0.03
	Reverse	6.52	1.38	0.72	6.48	
$InBr_3$: 0.27 M	Forward	5.95	1.35	0.66	5.30	0.08
	Reverse	6.01	1.37	0.70	5.76	

4. Conclusions

In the process of preparing the $CsPbBr_3$ film by the multi-step method, we introduced $InBr_3$ into the $PbBr_2$ precursor, so that the $PbBr_2$ film was transformed from a flat membrane to a porous membrane, which was beneficial to improve the reaction efficiency of CsBr and $PbBr_2$, reduced the impurity in $CsPbBr_3$, and optimized the surface morphology, and, finally, enabled the performance of $CsPbBr_3$ PSCs to be significantly improved. When combined with host lattices, the In^{3+} or In cluster could effectively suppress the carrier recombination in the $CsPbBr_3$ film and shift up the Ev of $CsPbBr_3$, thereby enhancing the charge extraction and transportation capabilities. When the $InBr_3$ concentration in the $PbBr_2$ precursor solution was 0.21 M, the $InBr_3$:$CsPbBr_3$ device presented the best photovoltaic performance with a PCE of 6.48% and, especially the V_{OC} significantly increased by 100 mV compared with the pristine $CsPbBr_3$. These research results confirmed that $InBr_3$ has solid potentials for improving the performance of $CsPbBr_3$ PSCs and also provided a reference for $InBr_3$ or some other metal bromide applications in the inorganic $CsPbI_3$ PSCs field and developmental direction.

Supplementary Materials: The following are available online at https://www.mdpi.com/article/10.3390/nano11051253/s1, Figure S1: Cross-sectional SEM images of $PbBr_2$ films by introducing

different concentrations of $InBr_3$: (a) 0.00 M; (b) 0.03 M; (c) 0.09 M; (d) 0.15 M; (e) 0.21 M; (f) 0.27 M; Figure S2: The SEM image of $InBr_3$:$PbBr_2$ film (a) and the corresponding EDS mapping of Pb (b), Br (c) and In (d); Figure S3: XPS spectra of $InBr_3$:$CsPbBr_3$ film; Figure S4: The cross-sectional SEM image of $InBr_3$:$CsPbBr_3$ film (a) and the corresponding EDS mapping of Cs (b), Pb (c), Br (d) and In (e); Figure S5: UV-vis absorption spectra (a) and $(\alpha h\nu)^2$ vs. $h\nu$ plots (b) of the modules by introducing different concentrations of $InBr_3$; Figure S6: *J–V* curves with forward and reverse voltage scanning for the $InBr_3$:$CsPbBr_3$ devices: (a) 0.00 M; (b) 0.03 M; (c) 0.09 M; (d) 0.15 M; (e) 0.21 M; (f) 0.27 M; Table S1: Electrochemical Impedance Spectroscopy parameters of the pristine and $InBr_3$ (0.21 M):$CsPbBr_3$ modules.

Author Contributions: K.C., H.Y. and W.F. conceived the idea; X.M. performed research, analyzed data, and wrote the paper; K.C., Q.L., B.F., P.Z., H.W. and T.G. provided assistance for data acquisition and data analysis. All authors have read and agreed to the published version of the manuscript.

Funding: This work was financially supported by the National Natural Science Foundation of China (No. 51272086) and Scientific Research Staring Foundation for the Doctors of the Northeast Electric Power University (No. BSJXM-2018223).

Conflicts of Interest: The authors declare no conflict of interest.

References

1. Kojima, A.; Teshima, K.; Shirai, Y.; Miyasaka, T. Organometal Halide Perovskites as Visible-Light Sensitizers for Photovoltaic Cells. *J. Am. Chem. Soc.* **2009**, *131*, 6050–6051. [CrossRef] [PubMed]
2. Chen, W.; Li, X.; Li, Y.; Li, Y. A review: Crystal growth for high-performance all-inorganic perovskite solar cells. *Energy Environ. Sci.* **2020**, *13*, 1971–1996. [CrossRef]
3. Park, N.-G.; Grätzel, M.; Miyasaka, T.; Zhu, K.; Emery, K. Towards stable and commercially available perovskite solar cells. *Nat. Energy* **2016**, *1*, 16152. [CrossRef]
4. Zhou, H.; Chen, Q.; Li, G.; Luo, S.; Song, T.-B.; Duan, H.-S.; Hong, Z.; You, J.; Liu, Y.; Yang, Y. Interface engineering of highly efficient perovskite solar cells. *Science* **2014**, *345*, 542–546. [CrossRef] [PubMed]
5. Jiang, Q.; Zhao, Y.; Zhang, X.; Yang, X.; Chen, Y.; Chu, Z.; Ye, Q.; Li, X.; Yin, Z.; You, J. Surface passivation of perovskite film for efficient solar cells. *Nat. Photonics* **2019**, *13*, 460–466. [CrossRef]
6. Wang, Q.; Zhang, X.; Jin, Z.; Zhang, J.; Gao, Z.; Li, Y.; Liu, S. Energy-Down-Shift $CsPbCl_3$:Mn Quantum Dots for Boosting the Efficiency and Stability of Perovskite Solar Cells. *ACS Energy Lett.* **2017**, *2*, 1479–1486. [CrossRef]
7. Park, B.; Seok, S.I. Intrinsic Instability of Inorganic–Organic Hybrid Halide Perovskite Materials. *Adv. Mater.* **2019**, *31*, e1805337. [CrossRef] [PubMed]
8. Zhang, J.; Hodes, G.; Jin, Z.; Liu, S. All-Inorganic $CsPbX_3$ Perovskite Solar Cells: Progress and Prospects. *Angew. Chem. Int. Ed.* **2019**, *58*, 15596–15618. [CrossRef]
9. Eperon, G.E.; Paternò, G.M.; Sutton, R.J.; Zampetti, A.; Haghighirad, A.A.; Cacialli, F.; Snaith, H.J. Inorganic caesium lead iodide perovskite solar cells. *J. Mater. Chem. A* **2015**, *3*, 19688–19695. [CrossRef]
10. Wang, Y.; Liu, X.; Zhang, T.; Wang, X.; Kan, M.; Shi, J.; Zhao, Y. The Role of Dimethylammonium Iodide in $CsPbI_3$ Perovskite Fabrication: Additive or Dopant? *Angew. Chem. Int. Ed.* **2019**, *58*, 16691–16696. [CrossRef]
11. Wang, H.; Dong, Z.; Liu, H.; Li, W.; Zhu, L.; Chen, H. Roles of Organic Molecules in Inorganic $CsPbX_3$ Perovskite Solar Cells. *Adv. Energy Mater.* **2021**, *11*, 2002940. [CrossRef]
12. Zeng, Q.; Zhang, X.; Liu, C.; Feng, T.; Chen, Z.; Zhang, W.; Zheng, W.; Zhang, H.; Yang, B. Inorganic $CsPbI_2$ Br Perovskite Solar Cells: The Progress and Perspective. *Sol. RRL* **2019**, *3*, 1800239. [CrossRef]
13. Duan, J.; Xu, H.; Sha, W.E.I.; Zhao, Y.; Wang, Y.; Yang, X.; Tang, Q. Inorganic perovskite solar cells: An emerging member of the photovoltaic community. *J. Mater. Chem. A* **2019**, *7*, 21036–21068. [CrossRef]
14. Faheem, M.B.; Khan, B.; Feng, C.; Farooq, M.U.; Raziq, F.; Xiao, Y.; Li, Y. All-Inorganic Perovskite Solar Cells: Energetics, Key Challenges, and Strategies toward Commercialization. *ACS Energy Lett.* **2020**, *5*, 290–320. [CrossRef]
15. Liang, J.; Wang, C.; Wang, Y.; Xu, Z.; Lu, Z.; Ma, Y.; Zhu, H.; Hu, Y.; Xiao, C.; Yi, X.; et al. All-Inorganic Perovskite Solar Cells. *J. Am. Chem. Soc.* **2016**, *138*, 15829–15832. [CrossRef] [PubMed]
16. Zhao, Z.; Gu, F.; Rao, H.; Ye, S.; Liu, Z.; Bian, Z.; Huang, C. Metal Halide Perovskite Materials for Solar Cells with Long-Term Stability. *Adv. Energy Mater.* **2019**, *9*, 1802671. [CrossRef]
17. Mariotti, S.; Hutter, O.S.; Phillips, L.J.; Yates, P.J.; Kundu, B.; DuRose, K. Stability and Performance of $CsPbI_2Br$ Thin Films and Solar Cell Devices. *ACS Appl. Mater. Interfaces* **2018**, *10*, 3750–3760. [CrossRef] [PubMed]
18. Li, Y.; Wang, Y.; Zhang, T.; Yoriya, S.; Kumnorkaew, P.; Chen, S.; Guo, X.; Zhao, Y. Li dopant induces moisture sensitive phase degradation of an all-inorganic $CsPbI_2Br$ perovskite. *Chem. Commun.* **2018**, *54*, 9809–9812. [CrossRef]
19. Akbulatov, A.F.; Luchkin, S.Y.; Frolova, L.A.; Dremova, N.N.; Gerasimov, K.L.; Zhidkov, I.S.; Anokhin, D.V.; Kurmaev, E.Z.; Stevenson, K.J.; Troshin, P.A. Probing the Intrinsic Thermal and Photochemical Stability of Hybrid and Inorganic Lead Halide Perovskites. *J. Phys. Chem. Lett.* **2017**, *8*, 1211–1218. [CrossRef] [PubMed]

20. Li, X.; Cao, F.; Yu, D.; Chen, J.; Sun, Z.; Shen, Y.; Zhu, Y.; Wang, L.; Wei, Y.; Wu, Y.; et al. All Inorganic Halide Perovskites Nanosystem: Synthesis, Structural Features, Optical Properties and Optoelectronic Applications. *Small* **2017**, *13*, 1603996. [CrossRef]
21. Tian, J.; Xue, Q.; Yao, Q.; Li, N.; Brabec, C.J.; Yip, H. Inorganic Halide Perovskite Solar Cells: Progress and Challenges. *Adv. Energy Mater.* **2020**, *10*, 2000183. [CrossRef]
22. Kulbak, M.; Gupta, S.; Kedem, N.; Levine, I.; Bendikov, T.; Hodes, G.; Cahen, D. Cesium Enhances Long-Term Stability of Lead Bromide Perovskite-Based Solar Cells. *J. Phys. Chem. Lett.* **2016**, *7*, 167–172. [CrossRef] [PubMed]
23. Zhao, Y.; Duan, J.; Wang, Y.; Yang, X.; Tang, Q. Precise stress control of inorganic perovskite films for carbon-based solar cells with an ultrahigh voltage of 1.622 V. *Nano Energy* **2020**, *67*, 104286. [CrossRef]
24. Rühle, S. The detailed balance limit of perovskite/silicon and perovskite/CdTe tandem solar cells. *Phys. Status Solidi* **2017**, *214*, 1600955. [CrossRef]
25. Duan, J.; Zhao, Y.; He, B.; Tang, Q. High-Purity Inorganic Perovskite Films for Solar Cells with 9.72% Efficiency. *Angew. Chem. Int. Ed.* **2018**, *57*, 3787–3791. [CrossRef]
26. Huang, D.; Xie, P.; Pan, Z.; Rao, H.; Zhong, X. One-step solution deposition of $CsPbBr_3$ based on precursor engineering for efficient all-inorganic perovskite solar cells. *J. Mater. Chem. A* **2019**, *7*, 22420–22428. [CrossRef]
27. Dong, C.; Han, X.; Li, W.; Qiu, Q.; Wang, J. Anti-solvent assisted multi-step deposition for efficient and stable carbon-based $CsPbI_2Br$ all-inorganic perovskite solar cell. *Nano Energy* **2019**, *59*, 553–559. [CrossRef]
28. Lee, E.J.; Kim, D.-H.; Chang, R.P.H.; Hwang, D.-K. Induced Growth of $CsPbBr_3$ Perovskite Films by Incorporating Metal Chalcogenide Quantum Dots in $PbBr_2$ Films for Performance Enhancement of Inorganic Perovskite Solar Cells. *ACS Appl. Energy Mater.* **2020**, *3*, 10376–10383. [CrossRef]
29. Tu, Y.; Wu, J.; He, X.; Guo, P.; Wu, T.; Luo, H.; Liu, Q.; Wang, K.; Lin, J.; Huang, M.; et al. Solvent engineering for forming stonehenge-like PbI_2 nano-structures towards efficient perovskite solar cells. *J. Mater. Chem. A* **2017**, *5*, 4376–4383. [CrossRef]
30. Cao, X.; Zhi, L.; Li, Y.; Fang, F.; Cui, X.; Yao, Y.; Ci, L.; Ding, K.; Wei, J. Control of the morphology of PbI_2 films for efficient perovskite solar cells by strong Lewis base additives. *J. Mater. Chem. C* **2017**, *5*, 7458–7464. [CrossRef]
31. McGarvey, B.R.; Trudell, C.O.; Tuck, D.G.; Victoriano, L. Coordination compounds of indium. 37. Indium-115 NMR studies of anionic indium species in nonaqueous solution. *Inorg. Chem.* **1980**, *19*, 3432–3436. [CrossRef]
32. Sayevich, V.; Guhrenz, C.; Sin, M.; Dzhagan, V.M.; Weiz, A.; Kasemann, D.; Brunner, E.; Ruck, M.; Zahn, D.R.T.; Leo, K.; et al. Chloride and Indium-Chloride-Complex Inorganic Ligands for Efficient Stabilization of Nanocrystals in Solution and Doping of Nanocrystal Solids. *Adv. Funct. Mater.* **2016**, *26*, 2163–2175. [CrossRef]
33. Lee, W.S.; Kang, Y.G.; Woo, H.K.; Ahn, J.; Kim, H.; Kim, D.; Jeon, S.; Han, M.J.; Choi, J.-H.; Oh, S.J. Designing High-Performance CdSe Nanocrystal Thin-Film Transistors Based on Solution Process of Simultaneous Ligand Exchange, Trap Passivation, and Doping. *Chem. Mater.* **2019**, *31*, 9389–9399. [CrossRef]
34. Wang, Z.-K.; Li, M.; Yang, Y.-G.; Hu, Y.; Ma, H.; Gao, X.-Y.; Liao, L.-S. High Efficiency Pb-In Binary Metal Perovskite Solar Cells. *Adv. Mater.* **2016**, *28*, 6695–6703. [CrossRef] [PubMed]
35. Liu, C.; Li, W.; Li, H.; Wang, H.; Zhang, C.; Yang, Y.; Gao, X.; Xue, Q.; Yip, H.-L.; Fan, J.; et al. Structurally Reconstructed $CsPbI_2$ Br Perovskite for Highly Stable and Square-Centimeter All-Inorganic Perovskite Solar Cells. *Adv. Energy Mater.* **2019**, *9*, 1803572. [CrossRef]
36. Liu, M.; Zhong, G.; Yin, Y.; Miao, J.; Clifton, S.; Wang, C.; Xu, X.; Jingsheng, M.; Meng, H. Aluminum-Doped Cesium Lead Bromide Perovskite Nanocrystals with Stable Blue Photoluminescence Used for Display Backlight. *Adv. Sci.* **2017**, *4*, 1700335. [CrossRef]
37. Liu, X.; Tan, X.; Liu, Z.; Ye, H.; Sun, B.; Shi, T.; Tang, Z.; Liao, G. Boosting the efficiency of carbon-based planar $CsPbBr_3$ perovskite solar cells by a modified multistep spin-coating technique and interface engineering. *Nano Energy* **2019**, *56*, 184–195. [CrossRef]
38. Swarnkar, A.; Mir, W.J.; Nag, A. Can B-Site Doping or Alloying Improve Thermal- and Phase-Stability of All-Inorganic $CsPbX_3$ (X = Cl, Br, I) Perovskites? *ACS Energy Lett.* **2018**, *3*, 286–289. [CrossRef]
39. Li, X.; He, B.; Gong, Z.; Zhu, J.; Zhang, W.; Chen, H.; Duan, Y.; Tang, Q. Compositional Engineering of Chloride Ions Doped $CsPbBr_3$ Halides for Highly Efficient and Stable All-Inorganic Perovskite Solar Cells. *Sol. RRL* **2020**, *4*, 2000362. [CrossRef]
40. He, J.; Su, J.; Ning, Z.; Ma, J.; Zhou, L.; Lin, Z.; Zhang, J.; Liu, S.; Chang, J.; Hao, Y. Improved Interface Contact for Highly Stable All-Inorganic $CsPbI_2Br$ Planar Perovskite Solar Cells. *ACS Appl. Energy Mater.* **2020**, *3*, 5173–5181. [CrossRef]
41. Chen, J.; Choy, W.C.H. Efficient and Stable All-Inorganic Perovskite Solar Cells. *Sol. RRL* **2020**, *4*, 2000408. [CrossRef]
42. Chen, L.; Wan, L.; Li, X.; Zhang, W.; Fu, S.; Wang, Y.; Li, S.; Wang, H.-Q.; Song, W.; Fang, J. Inverted All-Inorganic $CsPbI_2Br$ Perovskite Solar Cells with Promoted Efficiency and Stability by Nickel Incorporation. *Chem. Mater.* **2019**, *31*, 9032–9039. [CrossRef]